Nanomechanical Characterization of an Antiferromagnetic Topological Insulator

Shuwan Liu, Su Kong Chong, Dongwook Kim, Amit Vashist, Rohit Kumar, Seng Huat Lee, Kang L. Wang, Zhiqiang Mao, Feng Liu, and Vikram V. Deshpande*

Cite This: *Nano Lett.* 2025, 25, 973−980

Read Online

ACCESS | 📊 Metrics & More | 📰 Article Recommendations | 🔵 Supporting Information

ABSTRACT: The antiferromagnetic topological insulator $MnBi_2Te_4$ (MBT) exhibits an ideal platform for investigating unique topological and magnetic properties. While the transport characteristics of magnetic phase transitions in the MBT materials have been extensively studied, the understanding of their mechanical properties and magneto−mechanical coupling remains limited. Here, we utilize nanoelectromechanical systems to probe the intrinsic magnetism in MBT thin flakes through magnetostrictive coupling. By analyzing the mechanical resonance signatures, we explore the magnetic phase transitions from antiferromagnetic (AFM) to canted antiferromagnetic (CAFM) to ferromagnetic (FM) phases as a function of magnetic field. Our results reveal the spin-flop transitions in MBT, characterized by frequency shifts in the mechanical resonance. To establish a correlation between the frequency shifts and the spin-canting states, we employ a magnetostrictive model to extract the magnetostrictive coefficients. Our study demonstrates a valuable approach using nanoelectromechanical systems to investigate magnetic phase transitions, magnetization, and magnetoelastic properties in antiferromagnetic topological insulators.

KEYWORDS: Antiferromagnetic topological insulator, Nanoelectromechanical resonator, Magnetostriction, Spin-flop, Magnetic phase transition
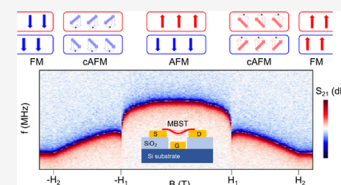
Nanoelectromechanical systems (NEMS) have found widespread applications in nano filtering, ultrahigh sensitivity mass/force/pressure sensing, and molecular detection. NEMS based on graphene and 2D materials have been extensively studied[1−9] for their high-performance characteristics, including ultralow mass density, exceptional mechanical flexibility, and stiffnesses. These 2D NEMS offer new opportunities for controlling mechanical, electrical, and optical properties across various degrees of freedom. For instance, they have been investigated for their optical properties and charge density wave transitions in transition-metal dichalcogenides,[10−12] as well as for magnetic phase transitions in antiferromagnetic and ferromagnetic materials.[13] Recently, researchers have leveraged field-induced magnetostriction[14−17] in magnetic 2D materials to achieve new control of magneto−mechanical coupling in NEMS.[18]

Another intriguing material in this field is the intrinsic magnetic topological insulator $MnBi_2Te_4$[19−21] (MBT), where spins are coupled intralayer in the ferromagnetic (FM) state, while interlayer coupling is antiferromagnetic (AFM). As an antiferromagnetic topological insulator, the MBT material family provides an excellent platform for studying new electronic and magnetic couplings with mechanical motion. The introduction of magnetism in the MBT leads to the emergence of exotic phenomena, including the quantum anomalous Hall effect,[22,23] axion insulator state[24,25] and layer Hall effect.[26] The band structures of the MBT compounds have been extensively studied using angle-resolved photo-

emission spectroscopy (ARPES),[20,27] revealing that MBT is a heavily electron-doped compound with the Fermi level residing in the conduction band. Recent investigations using first-principles calculations, ARPES and transport measurements have demonstrated that the Fermi level of $Mn(Bi_{1−x}Sb_x)_2Te_4$ can be tuned from the conduction band to the valence band by varying the Sb concentration (x).[28−30]

The study of spin−lattice coupling in magnetic topological insulators has the potential to enable the detection, control and modification of spin states and magnetic structures. Previous research on MBT films has underscored the importance of magnon−phonon interactions and substrate effects in magnetic phase transitions, as evidenced by Raman spectroscopy measurements.[31−33] Additionally, nanomechanical strain can be employed to detect magnetic states and their coupling with mechanical degrees of freedom. In this study, we focus on the exchange magnetostriction effect in $Mn(Bi_{0.8}Sb_{0.2})_2Te_4$ (MBST) films by constructing a NEM resonator device structure. This device design, featuring a suspended membrane geometry, eliminates interaction between the sample and the substrates, allowing for cleaner manifestations of phase
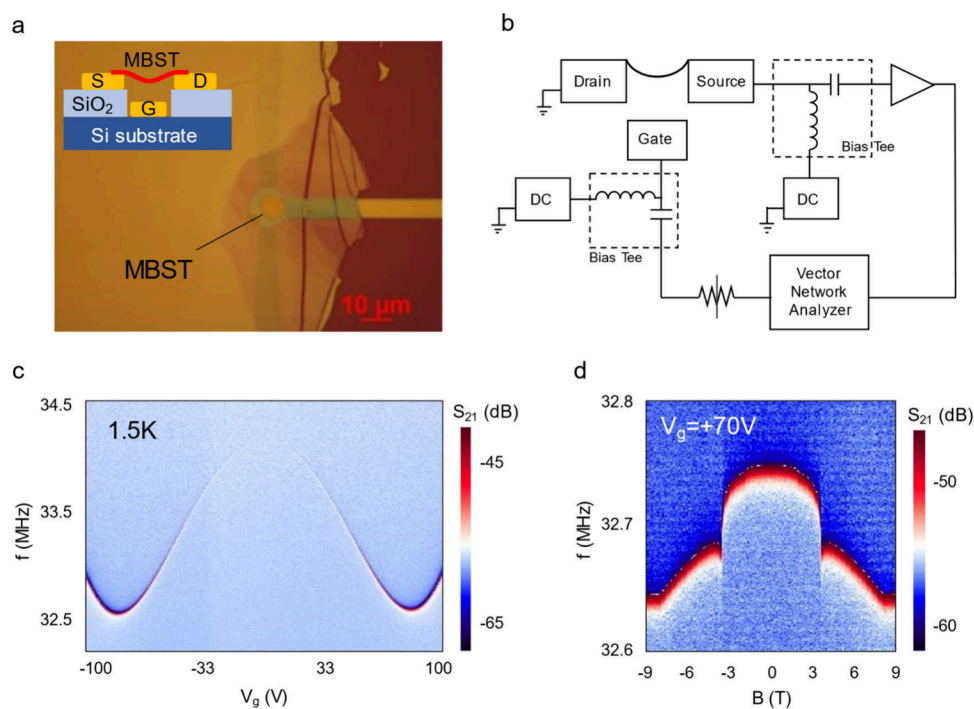
Figure 1. MBST NEM resonator. (a) Optical image of an MBST resonator device. Inset is a schematic of the side view of the device geometry. (b) Schematic of circuit setup for the radio frequency (RF) measurement. The RF excitation from the VNA output and DC voltage from the source measuring unit are combined through a bias tee and then applied to the gate electrode. The RF signals are fed back into the VNA input to generate the RF transmission S_{21}. (c) Gate dependence of f_{res} measured at 1.5 K. Color plot of S_{21} as functions of driving frequency and gate voltage. (d) Magnetic field dependence of f_{res} measured at a temperature of 1.5 K and gate voltage V_g = +70 V. Color plot of S_{21} as functions of driving frequency and out-of-plane magnetic field.

transitions.[34] The exchange magnetostriction in the antiferromagnetic topological insulator MBST responds to changes in the magnetization of the Mn layer, inducing magnetostrictive strain in the film. This strain, induced by the magnetostrictive effect, is reflected in changes in the resonance frequency (f_{res}) of the NEM resonator. By monitoring shifts in f_{res}, we can distinguish different magnetic states and gain insight into the transition between them, thereby enhancing our understanding of spin−lattice coupling. To further support these findings, we determine the magnetoelastic energy parameters from magnetic field dependent f_{res} measurements, which are corroborated by density functional theory (DFT) calculations.

The MBST NEM resonator devices were prepared following these steps:[35] (*i*) bottom gate gold electrodes (30 nm) were photolithographically patterned on a highly resistive silicon wafer (600 μm); (*ii*) a SiO$_2$ layer (300 nm) was deposited using plasma-enhanced chemical vapor deposition; (*iii*) source and drain gold leads (25 nm) were patterned and deposited as in (*i*); (*iv*) a circular hole was etched down to the bottom gate electrode via a dry reactive-ion etching process; and (*v*) MBST flakes were exfoliated and transferred onto the prepatterned gold leads over the circular hole using a micromanipulator transfer stage. Figure 1a displays an optical image of a representative MBST NEM resonator device, consisting of an MBST flake with a thickness of about 30 nm, suspended over a hole with a radius of 4 μm. The schematic in Figure 1a illustrates the side view of the device structure, where the MBST flake and the underneath gold gate electrode form a parallel capacitor structure with vacuum as the dielectric. The two-terminal resistance of the MBST flake typically falls within the range of a few kΩ at room temperature.

Our transduction technique employs a high-frequency electrical circuit to actuate and detect the mechanical resonances in the MBST resonator device. A DC voltage applied to the gate electrode induces static tension and displacement in the MBST flake while the AC voltage is used to modulate the displacement. This alters the capacitance between the MBST flake and the gate electrode, which gives rise to a large capacitive contribution to the transmission on resonance.[36]

The radio frequency (RF) measurements were conducted in a variable temperature insert at a base temperature of 1.5 K. Figure 1b illustrates the circuit diagram of the RF measurement setup. The mechanical vibrations were driven by an RF signal output from a vector network analyzer (VNA). This RF signal was coupled to a DC gate voltage through a bias tee, and the transmitted RF signal was decoupled using a second bias tee before being fed back to the VNA. The fundamental resonance mode of the MBST membrane was fitted to a Fano line shape with a peak frequency of about 32.7 MHz, exhibiting a quality factor (Q) exceeding 5000 (Supporting Information, Figure S1). This Q-value is comparable to those observed in other 2D magnet resonators[13,37,38] and is similar to high-quality resonator made from graphene[39] and WSe$_2$.[40] Figure 1c presents a color plot of the RF transmission (S_{21}) signal as a function of frequency and gate voltage. The gate voltage (V_g) generates an electrostatic force that induce mechanical tension in the MBST membrane, shifting its resonance frequencies (f_{res}). The f_{res} decreases to a minimum at $V_g \sim \pm 80$ V due to capacitive softening and then increases with a further increase in $|V_g|$ due to gate-induced stiffening, similar to other NEMS.[41] The gate-dependent f_{res} were fitted using a continuum mechanics model[36] for a fully clamped membrane, as discussed

in Supporting Information 2 and 3. The fitted curve is shown as a solid black line in Supporting Information 4, Figure S2. The input parameters for the fit obtained from DFT calculations for the MBST, including Young's modulus, mass density, and Poisson's ratio, are summarized in Table 1. Based

Table 1. Summary of the Physical, Mechanical, and Magnetostrictive Parameters Obtained from DFT Calculations and Fitting to the RF Experimental Data for the MBST NEM Resonator

	Experiment	DFT
Mass density (kg/m^3)	-	7360
Young's modulus, E (GPa)	-	84.374
Poisson's ratio, v_P	-	0.212
Built-in strain, ϵ_0 (%)	0.83	-
Built-in-stress, σ_0 (N/m)	88.24	-
Magnetostrictive coefficients (meV): $A_u \frac{\partial J_\perp}{\partial \epsilon}$	9	2.8
$A_u \frac{\partial K_{eff}}{\partial \epsilon}$	0.6	0.195

on these parameters, we estimate a built-in strain $\epsilon_0 \approx 0.83\%$ in the MBST NEM resonator device. The relatively large ϵ_0, compared to other resonator systems,[13,37,38] is consistent with its "W"-shaped $f_{res}(V_g)$ curve (Figure 1c), similar to high ϵ_0 graphene[39] and MoS$_2$[42] based resonators.

Next, we investigate the effect of magnetic field on the f_{res} for the MBST NEMS device. Due to the weak interlayer antiferromagnetic coupling, MBST device undergoes magnetic transitions under a perpendicular magnetic field. Figure 1d presents a color plot of S$_{21}$ as a function of frequency and magnetic field, with V_g fixed at 70 V. We observe two distinct transitions in the magnetic field. The first transition is characterized by a jump in f_{res} at around 3.7 T, while the second transition occurs at around 8 T, where the f_{res} saturates with increasing magnetic field. These observed transitions in f_{res} align with the magnetic phase transitions reported in previous studies on MBST.[27,34,43] Specifically, the first transition corresponds to a spin-flop process from AFM to

the canted antiferromagnetic (CAFM) phase, while the second transition corresponds to the transition from CAFM to the FM phase. Consistently, we have observed similar results in all of the fabricated MBST resonator devices that have been measured thus far (see Supporting Information 8, Figure S6 for additional data).

To further verify the field-induced magnetic phase transitions, we performed magnetotransport measurements on MBST devices. MBST flakes of similar thickness were fabricated into Hall bar devices using a standard electron beam lithography, with a Cr/Au contact electrode deposited in a thickness of 10/60 nm. The top gate was made by transferring hBN and graphite layers to serve as the dielectric and gate electrode, respectively, onto the Hall bar devices. Figures 2a and b show the gate and magnetic field dependent R$_{xx}$ and R$_{yx}$ for a 30 nm MBST Hall bar device (Figure 2d, inset). Line cuts of R$_{xx}$ and R$_{yx}$ were taken at different temperatures in the two distinct Hall signal regions: V_{tg} of +7.8 V (hole carrier) and +16.5 V (charge neutrality), as shown in Figures 2c−f. The discontinuous vertical steps observed in the R$_{xx}$ color map at ±2.8 T are assigned to the spin-flop transition field (H$_1$), which corresponds to the transition from AFM to CAFM states. Similarly, the second turning point in the R$_{yx}$ curves indicates the saturation field (H$_2$), corresponding to the transition from CAFM to FM states. As temperature increases, the kink observed in R$_{xx}$ diminishes and eventually disappears at 25 K, which is consistent with the Néel temperature $T_N \sim$ 23 K[43,44] of the MBST. The blue and red arrows in Figures 2c−f track the evolution of H$_1$ and H$_2$ with temperature for the two carrier densities, respectively (refer to Supporting Information 6, Figure S4 for the full data set). Notably, the magnetotransport analyses indicate that H$_1$ and H$_2$ are nearly independent of the gate voltages, thereby excluding the possibility of carrier density modulated magnetic transitions in MBST.

Our NEM resonator devices demonstrate a clear relationship between the f_{res} and the magnetic transitions. In Figures 3a−e, we present the magnetic field dependent S$_{21}$ measurements for the MBST resonator device at various temperatures. The
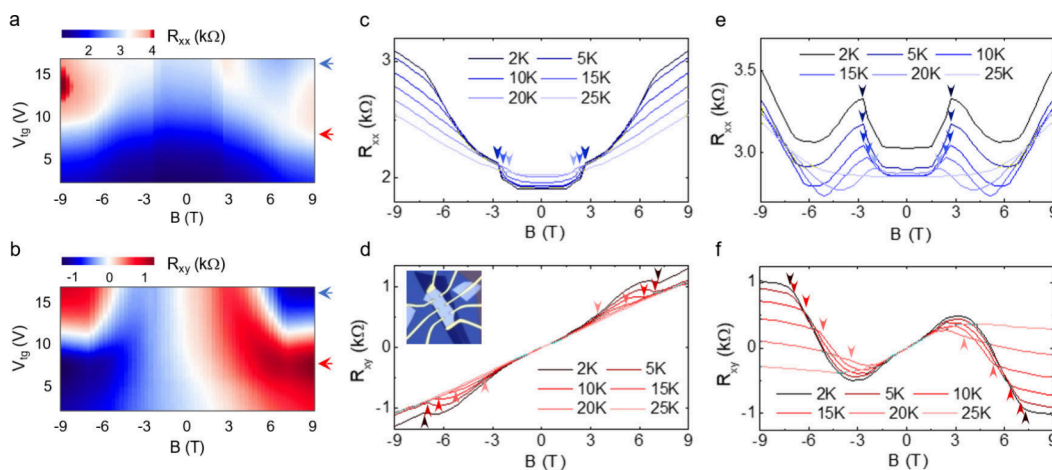

Figure 2. MBST Hall bar device. Color plots of (a) R$_{xx}$ and (b) R$_{yx}$ as functions of magnetic field and gate voltage for a 30 nm thick MBST flake. The data were taken at a temperature of 2 K. The blue and red horizontal arrows point to the top-gate voltages where the line cuts are taken. Plots of (c) R$_{xx}$ and (d) R$_{yx}$ as a function magnetic field taken at different temperatures with the top-gate voltage fixed to +7.8 V. Inset in (d) is the optical image of the MBST device. Plots of (e) R$_{xx}$ and (f) R$_{yx}$ as a function magnetic field taken at different temperatures with the top-gate voltage fixed to +16.5 V. The R$_{xx}$ and R$_{yx}$ line profiles are symmetrized and antisymmetrized, respectively. Vertical arrows in (c,e) and (d,f) point to the H$_1$ and H$_2$, respectively, at different temperatures.
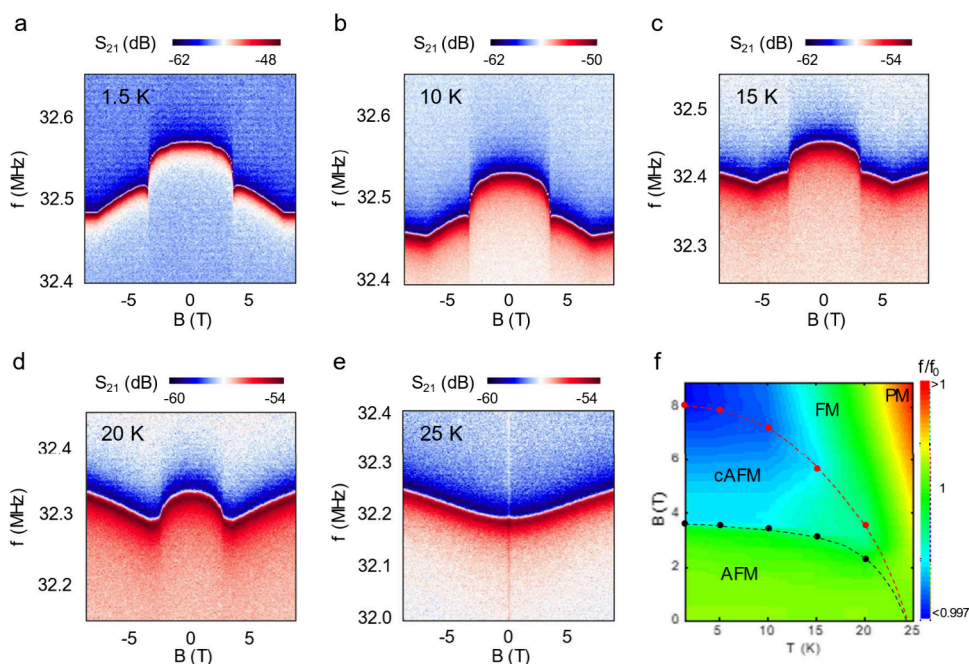
Figure 3. Temperature dependence of magnetic phase transition probed by resonance frequency. Color plots of RF transmission signal S_{21} as functions of driving frequency and magnetic field at a fixed gate voltage of +85 V at different temperatures of (a) 1.5 K, (b) 10 K, (c) 15 K, (d) 20 K, and (e) 25 K. (f) Magnetic phase diagram derived from the f_{res}. Color plot of $f_{res}(B)/f_{res}(0)$ as functions of magnetic field and temperature. The different magnetic phases of PM, AFM, CAFM, and FM states are labeled in the phase diagram.

disappearance of the transitions beyond the Neel temperature $T_N \sim 23$ K confirms the correlation between f_{res} and the magnetic transitions. Similar to our transport analysis, both H_1 and H_2 exhibit suppression with increasing temperature, albeit at different rates. The evolution of H_1 and H_2 with temperature below T_N, based on the change in f_{res}, is summarized in Supporting Information 5, Figure S3. At 25 K, we observe a monotonic increase in f_{res} with the magnetic field, suggesting the absence of long-range magnetic (spin) order, which is characteristic of a paramagnetic (PM) state. Notably, even at 10 K, f_{res} is no longer saturates at high field; instead, it increases linearly with the magnetic field beyond H_2. The positive slope in f_{res} follows a similar trend to the magnetic field dependent f_{res} observed at 25 K. This indicates that the magnetic field does not prolong the FM state at higher temperature, consistent with observations from magnetic force microscopy.[45] In contrast, the magnetic field dependent f_{res} exhibits consistent behavior in the AFM and CAFM phases at different temperatures, indicating a robust AFM ground state in the MBST. At higher temperatures, the PM phase dominates the high magnetic field regime, while the CAFM phase is nearly suppressed. By extracting the f_{res} data, we construct a magnetic phase diagram that incorporates the dependence on magnetic field and temperature, as shown in Figures 3a−e. Figure 3f presents a 2D color plot of the normalized resonance frequency, $f_{res}(B)/f_{res}(0)$, as a function of the magnetic field and temperature. The three magnetic phases, viz., AFM, CAFM, and FM states, are indicated for $T < T_N$, while the PM phase emerges at high temperature ($T > T_N$). The strong dependence of f_{res} on both magnetic field and temperature provides robust support for the magnetic phase transition picture in the MBST sample.

The dependence of f_{res} on the magnetic field indicates a magnetostrictive resonance. The mechanical resonance is correlated with the internal magnetic order, which changes

with the external magnetic field. The f_{res} reveals an abrupt change of about 0.32%, or equivalent to a Δf_{res} of 105 kHz, around the H_1 at the base temperature. Beyond the spin-flop transition ($H > H_1$), the f_{res} changes gradually with the magnetic field, eventually saturating at H_2. This behavior in CAFM state is absent in other 2D AFM materials, such as CrI_3[18] and $CrOCl$[38] resonators, indicating a correlation between Δf_{res} and the canting angle of the spins. To quantify the spin−lattice coupling, we employ the magnetostriction model[18] to fit our experimental data. According to this model, the shift in f_{res} with the magnetic state results from the competition between internal magnetic energy and elastic energy. The free energies per unit area for a freestanding membrane in the AFM, CAFM, and FM states in the zero-temperature limit can be expressed as

AFM state:

$$F_{AFM} = nF_0 + (n - 1)J_\perp \tag{1}$$

CAFM state:

$$F_{CAFM} = nF_0 + (n - 1)J_\perp \cos\theta + \frac{1}{2}nK_{eff}\sin^2\theta \tag{2}$$

FM state:

$$F_{FM} = nF_0 - (n - 1)J_\perp - \mu_0 M_0\left(H_\perp - \frac{M_0}{t}\right) \tag{3}$$

where θ is the canting angle of the spin of Mn atoms, n is the number of Mn layer, $J_\perp$ is the interlayer exchange in units of energy per unit area, and K_{eff} is the anisotropy in units of energy per unit area. The total energy of the MBST membrane is thus the sum of the free energy of the membrane, the elastic energy and the boundary energy of the fully clamped drum. The elastic energy and the boundary energy of the membrane per unit area can be expressed as $U_{el} = -\frac{1}{2}\sigma_0\epsilon$ and $U_b = -\sigma_0\epsilon$,
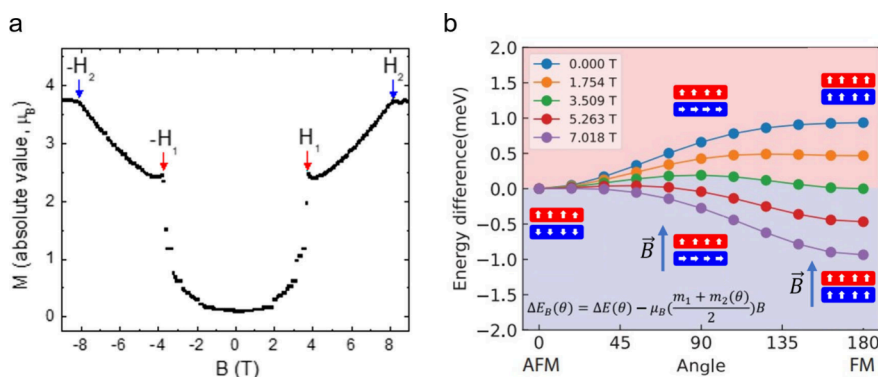
Figure 4. Resonance frequency derived magnetization and magnetostrictive effect in MBST. Effect of external magnetic field inducing the magnetic phase transition of MBST. (a) Magnetization (absolute value) per Mn atom as a function of out-of-plane magnetic field extracted from the f_{res}. The spin-flop field H_1 and saturation field H_2 are indicated in the figure. (b) DFT calculated relative energy of magnetic configuration as a function of spin angle in the bottom layer under the external magnetic field. Inset is a schematic of the Mn spin structure with the spin alignment angle for two septule layer MBSTs. Zero energy is set to the AFM ground state without an external field. The effect of the external magnetic field is described by the energy equation in (b).

respectively, where ϵ is the strain and σ_0 is the built-in stress. By taking the derivative of the total energy with respect to strain and setting this derivative equation to zero to minimize total energy, we can derive the frequency changes between AFM state, cAFM state, and FM state as a function of the magnetostrictive coefficients and the spin canting angle. Using unit cell area $A_u \approx 0.16$ nm^2 and $n = 31$ Mn layers corresponding to a reasonable estimate for the thickness (42 nm) of the sample, we obtain one magnetostrictive coefficient: $\frac{\partial J_\perp}{\partial \epsilon} A_u \approx 9$ meV. By comparing the fractional change of f_{res} in the canted AFM state and AFM state, we obtain the other magnetostrictive coefficient: $\frac{\partial K_{eff}}{\partial \epsilon} A_u \approx 0.6$ meV (Supporting Information 9). Using the values of the two magnetostrictive coefficients obtained above, we can fit the f_{res} as a dependence of magnetization. Figure 4a illustrates the correspondence between f_{res} and the absolute value of magnetization for the MBST as a function of the magnetic field. At low magnetic fields, the magnetization is almost zero. As the magnetic field approaches H_1, there is a dramatic increase in magnetization. The magnetization increases monotonically with the magnetic field in the CAFM state and ultimately saturates in the FM state. The strong consistency between the f_{res}-correlated magnetization and the literature[27,34,43] demonstrates the sensitivity of mechanical detection to magnetic states and their transitions.

To supplement the experimental results, we employ the DFT calculations to study the stability of the magnetic phases and to determine theoretical estimates for the magnetoelastic coefficients. Figure 4b plots the relative magnetic energy, $\Delta E_B(\theta)$, versus the spin alignment angle for a two septule layer MnBi$_{1.5}$Sb$_{0.5}$Te$_4$ under the different external magnetic fields. The relative energy, $\Delta E(\theta)$, for the AFM and FM configurations is obtained by manipulating the spin angle adjacent to the nearest spin layer, θ, as illustrated in the atomic lattice structures included in Figure 4b. The effect of the external magnetic field is incorporated by adding an energy gain term as $-\mu_B \left(\frac{m_{1,z} + m_{2,z}(\theta)}{2} \right) B$, where indexes 1 and 2 refer to the top and bottom septule layer, respectively. At 0 T, the relative magnetic energy is minimized in the AFM ground state. As the external magnetic field increases, the energy of the spins aligned with the external field decreases, as indicated by

the dotted colored lines in Figure 4b. Above the critical field ($B_c = 3.509$ T, green line), the relative magnetic energy of the FM state becomes negative, indicating that the FM state becomes energetically favorable compared to the AFM state. Subsequently, we show the magnetostriction effect due to in-plane tensile strain ($\epsilon > 0$) applied to the MBST system using DFT calculations. The changes in strain of the interlayer exchange coupling and magnetic anisotropic energies are obtained by

$$\frac{\partial J_\perp}{\partial \epsilon} = \frac{\partial}{\partial \epsilon}(E_{FM} - E_{AFM,z}) \tag{4}$$

$$\frac{\partial K_{eff}}{\partial \epsilon} = \frac{\partial}{\partial \epsilon}(E_{AFM,x} - E_{AFM,z}) \tag{5}$$

where E_{FM}, $E_{AFM,x}$, and $E_{AFM,z}$ denote the total energies of FM, x-directed AFM, and z-directed AFM phases. Increasing in-plane strain reduces the interlayer distance due to the Poisson ratio, resulting in a stronger interlayer exchange coupling. Using the built-in strain of 0.83% estimated from the experiments, we obtain the derivative of exchange and anisotropy with respect to strain for the MBST as $\frac{\partial J_\perp}{\partial \epsilon} Au \approx 2.8$ meV and $\frac{\partial K_{eff}}{\partial \epsilon} Au \approx 0.2$ meV (Supporting Information 10, Figure S7). The experimental and theoretical results for the two magnetostrictive coefficients are fairly consistent, with the interlayer exchange coupling in the few meV range and the anisotropy energy being 1 order of magnitude smaller. These magnetostrictive coefficients are also comparable to those found in other 2D antiferromagnets, such as CrI$_3$[18] and CrOCl.[38]

In summary, we have observed an exchange magneto-striction effect in the antiferromagnetic topological insulator MBST. We studied the mechanical properties of MBST NEM resonator and obtained key mechanical parameters, such as the elastic modulus, built-in strain, and Q-factor. The resonance frequency was highly responsive to changes in the external magnetic field, indicating the presence of magneto−mechanical coupling in MBST. The magnetostrictive behavior of the suspended MBST film provided insights into different magnetic states within the magnetic phase diagrams. We developed a modified magnetostriction model that accurately describes the spin flop transition in the CAFM state of MBST,

allowing us to extract the magnetization as a function of the magnetic field from the mechanical resonance measurements. Our results provide quantitative evidence for the correlation between intrinsic magnetic ordering and resonance frequency in MBST. Additionally, we quantified the exchange and anisotropy energies associated with strain using the magnetostriction model. Overall, our findings demonstrate the potential of the MBST-based NEM resonator structure as a new platform for exploring the inherent magnetism of MBT family materials.

METHODS

Crystal Growth. Bulk crystals of $Mn(Bi_{1-x}Sb_x)_2Te_4$ were synthesized using the Te-flux method.[29] The manganese powder, bismuth shot, antimony shot, and tellurium lumps with a molar ratio of $1:5(1-x):5x:16$ were loaded in an alumina crucible and sealed in a quartz tube under a high vacuum. The mixture was heated to 900 °C for 12 h to promote the homogeneous melting and slowly cooled down to a temperature window of 590 to 630 °C at a rate of 1.5 °C/h. The platelike single crystals can be obtained after removing the excess Bi−Te flux by centrifugation.

DFT Calculations. The first-principles calculations are performed within the framework of density functional theory (DFT) by Vienna an-initio calculation package (VASP)[46] in Perdew−Burke−Ernzerhof-type (PBE) generalized gradient approximation (GGA).[47] To address the electron correlation due to the Mn 3d orbitals, we include a Hubbard $U-J$ parameter 4 eV. The energy cutoff for the plane-wave basis is set to 450 eV, and K-point sampling is done using a $12 \times 12 \times 2$ Monkhorst−Pack grid.[48] All the crystal structures are fully relaxed until the atomic forces are below $1e^{-2}$ eV/Å. vdW correction is included by the DFT-D3 method[49] to better describe the interlayer dispersion forces.

ASSOCIATED CONTENT

Ⓢ Supporting Information

The Supporting Information is available free of charge at https://pubs.acs.org/doi/10.1021/acs.nanolett.4c04086.

Additional experimental details, DFT calculations, magnetotransport and resonance frequency data, and continuum mechanics model and exchange magnetostriction model (PDF)

AUTHOR INFORMATION

Corresponding Author

Vikram V. Deshpande − *Department of Physics and Astronomy, University of Utah, Salt Lake City, Utah 84112, United States;* ⓞ orcid.org/0000-0001-7681-0833; Phone: 801-581-6570; Email: vdesh@physics.utah.edu

Authors

Shuwan Liu − *Department of Physics and Astronomy, University of Utah, Salt Lake City, Utah 84112, United States;* ⓞ orcid.org/0000-0003-2184-9065

Su Kong Chong − *Department of Electrical and Computer Engineering, and Department of Physics and Astronomy, University of California, Los Angeles, California 90095, United States*

Dongwook Kim − *Department of Materials Science and Engineering, University of Utah, Salt Lake City, Utah 84112, United States*

Amit Vashist − *Department of Physics and Astronomy, University of Utah, Salt Lake City, Utah 84112, United States*

Rohit Kumar − *Department of Physics and Astronomy, University of Utah, Salt Lake City, Utah 84112, United States*

Seng Huat Lee − *Department of Physics and 2D Crystal Consortium, Materials Research Institute, The Pennsylvania State University, University Park, Pennsylvania 16802, United States*

Kang L. Wang − *Department of Electrical and Computer Engineering, and Department of Physics and Astronomy, University of California, Los Angeles, California 90095, United States;* ⓞ orcid.org/0000-0003-0487-5464

Zhiqiang Mao − *Department of Physics and 2D Crystal Consortium, Materials Research Institute, The Pennsylvania State University, University Park, Pennsylvania 16802, United States;* ⓞ orcid.org/0000-0002-4920-3293

Feng Liu − *Department of Materials Science and Engineering, University of Utah, Salt Lake City, Utah 84112, United States;* ⓞ orcid.org/0000-0002-3701-8058

Complete contact information is available at:
https://pubs.acs.org/10.1021/acs.nanolett.4c04086

Author Contributions

S.W.L. performed the measurements, analyzed the data, and cowrote the manuscript under the supervision of V.V.D.; S.K.C. helped with sample preparation and performed the transport measurements under the supervision of K.L.W.; D.K. performed DFT calculations under the supervision of F.L.; A.V. helped with measurements; R.K. fabricated the substrates; S.H.L. grew and characterized the crystal under the supervision of Z.Q.M.; all authors viewed and commented on the manuscript; and V.V.D. supervised the whole project.

Notes

The authors declare no competing financial interest.

ACKNOWLEDGMENTS

REFERENCES

(1) Bunch, J. S.; van der Zande, A. M.; Verbridge, S. S.; Frank, I. W.; Tanenbaum, D. M.; Parpia, J. M.; Craighead, H. G.; McEuen, P. L. Electromechanical Resonators from Graphene Sheets. *Science* **2007**, *315* (5811), 490−493.

(2) Garcia-Sanchez, D.; van der Zande, A. M.; Paulo, A. S.; Lassagne, B.; McEuen, P. L.; Bachtold, A. Imaging Mechanical Vibrations in Suspended Graphene Sheets. *Nano Lett.* **2008**, *8* (5), 1399−1403.

(3) Singh, V.; Sengupta, S.; Solanki, H. S.; Dhall, R.; Allain, A.; Dhara, S.; Pant, P.; Deshmukh, M. M. Probing Thermal Expansion of Graphene and Modal Dispersion at Low-Temperature Using Graphene Nanoelectromechanical Systems Resonators. *Nanotechnology* **2010**, *21* (16), 165204.

(4) van der Zande, A. M.; Barton, R. A.; Alden, J. S.; Ruiz-Vargas, C. S.; Whitney, W. S.; Pham, P. H. Q.; Park, J.; Parpia, J. M.; Craighead, H. G.; McEuen, P. L. Large-Scale Arrays of Single-Layer Graphene Resonators. *Nano Lett.* **2010**, *10* (12), 4869–4873.

(5) Eichler, A.; Moser, J.; Chaste, J.; Zdrojek, M.; Wilson-Rae, I.; Bachtold, A. Nonlinear Damping in Mechanical Resonators Made from Carbon Nanotubes and Graphene. *Nat. Nanotechnol.* **2011**, *6* (6), 339–342.

(6) Song, X.; Oksanen, M.; Sillanpää, M. A.; Craighead, H. G.; Parpia, J. M.; Hakonen, P. J. Stamp Transferred Suspended Graphene Mechanical Resonators for Radio Frequency Electrical Readout. *Nano Lett.* **2012**, *12* (1), 198–202.

(7) Changyao Chen; Hone, J. Graphene Nanoelectromechanical Systems. *Proc. IEEE* **2013**, *101* (7), 1766–1779.

(8) Chen, C.; Lee, S.; Deshpande, V. V.; Lee, G.-H.; Lekas, M.; Shepard, K.; Hone, J. Graphene Mechanical Oscillators with Tunable Frequency. *Nat. Nanotechnol.* **2013**, *8* (12), 923–927.

(9) Will, M.; Hamer, M.; Müller, M.; Noury, A.; Weber, P.; Bachtold, A.; Gorbachev, R. V.; Stampfer, C.; Güttinger, J. High Quality Factor Graphene-Based Two-Dimensional Heterostructure Mechanical Resonator. *Nano Lett.* **2017**, *17* (10), 5950–5955.

(10) Morell, N.; Reserbat-Plantey, A.; Tsioutsios, I.; Schädler, K. G.; Dubin, F.; Koppens, F. H. L.; Bachtold, A. High Quality Factor Mechanical Resonators Based on WSe$_2$ Monolayers. *Nano Lett.* **2016**, *16* (8), 5102–5108.

(11) Lee, J.; Wang, Z.; He, K.; Shan, J.; Feng, P. X.-L. High Frequency MoS$_2$ Nanomechanical Resonators. *ACS Nano* **2013**, *7* (7), 6086–6091.

(12) Sengupta, S.; Solanki, H. S.; Singh, V.; Dhara, S.; Deshmukh, M. M. Electromechanical Resonators as Probes of the Charge Density Wave Transition at the Nanoscale in NbSe 2. *Phys. Rev. B* **2010**, *82* (15), 155432.

(13) Šiškins, M.; Lee, M.; Mañas-Valero, S.; Coronado, E.; Blanter, Y. M.; van der Zant, H. S. J.; Steeneken, P. G. Magnetic and Electronic Phase Transitions Probed by Nanomechanical Resonators. *Nat. Commun.* **2020**, *11* (1), 2698.

(14) du DeLacheisserie, E.; de Lacheisserie, E. D. T. *Magnetostriction Theory and Applications of Magnetoelasticity*; CRC-Press, 1993.

(15) Diguet, G.; Sebald, G.; Nakano, M.; Lallart, M. N.; Cavaillé, J.-Y. Optimization of Magneto-Rheological Elastomers for Energy Harvesting Applications. *Smart Mater. Struct.* **2020**, *29* (7), 075017.

(16) Olabi, A. G.; Grunwald, A. Design and Application of Magnetostrictive Materials. *Mater. Des.* **2008**, *29* (2), 469–483.

(17) Fei, F.; Mao, Y.; Fang, W.; Liu, W.; Rollins, J. P.; Kondusamy, A. L. N.; Lv, B.; Ping, Y.; Wang, Y.; Xiao, J. Spin-Mechanical Coupling in 2D Antiferromagnet CrSBr. *Nano Lett.* **2024**, *24* (34), 10467–10474.

(18) Jiang, S.; Xie, H.; Shan, J.; Mak, K. F. Exchange Magnetostriction in Two-Dimensional Antiferromagnets. *Nat. Mater.* **2020**, *19* (12), 1295–1299.

(19) Gong, Y.; Guo, J.; Li, J.; Zhu, K.; Liao, M.; Liu, X.; Zhang, Q.; Gu, L.; Tang, L.; Feng, X.; Zhang, D.; Li, W.; Song, C.; Wang, L.; Yu, P.; Chen, X.; Wang, Y.; Yao, H.; Duan, W.; Xu, Y.; Zhang, S.-C.; Ma, X.; Xue, Q.-K.; He, K. Experimental Realization of an Intrinsic Magnetic Topological Insulator. *Chin. Phys. Lett.* **2019**, *36* (7), 076801.

(20) Otrokov, M. M.; Klimovskikh, I. I.; Bentmann, H.; Estyunin, D.; Zeugner, A.; Aliev, Z. S.; Gaß, S.; Wolter, A. U. B.; Koroleva, A. V.; Shikin, A. M.; Blanco-Rey, M.; Hoffmann, M.; Rusinov, I. P.; Vyazovskaya, A. Y.; Eremeev, S. V.; Koroteev, Y. M.; Kuznetsov, V. M.; Freyse, F.; Sánchez-Barriga, J.; Amiraslanov, I. R.; Babanly, M. B.; Mamedov, N. T.; Abdullayev, N. A.; Zverev, V. N.; Alfonsov, A.; Kataev, V.; Büchner, B.; Schwier, E. F.; Kumar, S.; Kimura, A.; Petaccia, L.; Di Santo, G.; Vidal, R. C.; Schatz, S.; Kißner, K.; Ünzelmann, M.; Min, C. H.; Moser, S.; Peixoto, T. R. F.; Reinert, F.; Ernst, A.; Echenique, P. M.; Isaeva, A.; Chulkov, E. V. Prediction and Observation of an Antiferromagnetic Topological Insulator. *Nature* **2019**, *576* (7787), 416–422.

(21) Li, J.; Li, Y.; Du, S.; Wang, Z.; Gu, B.-L.; Zhang, S.-C.; He, K.; Duan, W.; Xu, Y. Intrinsic Magnetic Topological Insulators in van Der Waals Layered MnBi2Te4-Family Materials. *Sci. Adv.* **2019**, *5* (6), No. eaaw5685.

(22) Deng, Y.; Yu, Y.; Shi, M. Z.; Guo, Z.; Xu, Z.; Wang, J.; Chen, X. H.; Zhang, Y. Quantum Anomalous Hall Effect in Intrinsic Magnetic Topological Insulator MnBi$_2$Te$_4$. *Science* **2020**, *367* (6480), 895–900.

(23) Deng, H.; Chen, Z.; Wołoś, A.; Konczykowski, M.; Sobczak, K.; Sitnicka, J.; Fedorchenko, I. V.; Borysiuk, J.; Heider, T.; Pluciński, Ł.; Park, K.; Georgescu, A. B.; Cano, J.; Krusin-Elbaum, L. High-Temperature Quantum Anomalous Hall Regime in a MnBi2Te4/Bi2Te3 Superlattice. *Nat. Phys.* **2021**, *17* (1), 36–42.

(24) Liu, C.; Wang, Y.; Li, H.; Wu, Y.; Li, Y.; Li, J.; He, K.; Xu, Y.; Zhang, J.; Wang, Y. Robust Axion Insulator and Chern Insulator Phases in a Two-Dimensional Antiferromagnetic Topological Insulator. *Nat. Mater.* **2020**, *19* (5), 522–527.

(25) Zhang, D.; Shi, M.; Zhu, T.; Xing, D.; Zhang, H.; Wang, J. Topological Axion States in the Magnetic Insulator MnBi 2 Te 4 with the Quantized Magnetoelectric Effect. *Phys. Rev. Lett.* **2019**, *122* (20), 206401.

(26) Gao, A.; Liu, Y.-F.; Hu, C.; Qiu, J.-X.; Tzschaschel, C.; Ghosh, B.; Ho, S.-C.; Bérubé, D.; Chen, R.; Sun, H.; Zhang, Z.; Zhang, X.-Y.; Wang, Y.-X.; Wang, N.; Huang, Z.; Felser, C.; Agarwal, A.; Ding, T.; Tien, H.-J.; Akey, A.; Gardener, J.; Singh, B.; Watanabe, K.; Taniguchi, T.; Burch, K. S.; Bell, D. C.; Zhou, B. B.; Gao, W.; Lu, H.-Z.; Bansil, A.; Lin, H.; Chang, T.-R.; Fu, L.; Ma, Q.; Ni, N.; Xu, S.-Y. Layer Hall Effect in a 2D Topological Axion Antiferromagnet. *Nature* **2021**, *595* (7868), 521–525.

(27) Lee, S. H.; Zhu, Y.; Wang, Y.; Miao, L.; Pillsbury, T.; Yi, H.; Kempinger, S.; Hu, J.; Heikes, C. A.; Quarterman, P.; Ratcliff, W.; Borchers, J. A.; Zhang, H.; Ke, X.; Graf, D.; Alem, N.; Chang, C.-Z.; Samarth, N.; Mao, Z. Spin Scattering and Noncollinear Spin Structure-Induced Intrinsic Anomalous Hall Effect in Antiferromagnetic Topological Insulator MnB i 2 T e 4. *Phys. Rev. Res.* **2019**, *1* (1), 012011.

(28) Chen, B.; Fei, F.; Zhang, D.; Zhang, B.; Liu, W.; Zhang, S.; Wang, P.; Wei, B.; Zhang, Y.; Zuo, Z.; Guo, J.; Liu, Q.; Wang, Z.; Wu, X.; Zong, J.; Xie, X.; Chen, W.; Sun, Z.; Wang, S.; Zhang, Y.; Zhang, M.; Wang, X.; Song, F.; Zhang, H.; Shen, D.; Wang, B. Intrinsic Magnetic Topological Insulator Phases in the Sb Doped MnBi2Te4 Bulks and Thin Flakes. *Nat. Commun.* **2019**, *10* (1), 4469.

(29) Lee, S. H.; Graf, D.; Min, L.; Zhu, Y.; Yi, H.; Ciocys, S.; Wang, Y.; Choi, E. S.; Basnet, R.; Fereidouni, A.; Wegner, A.; Zhao, Y.-F.; Verlinde, K.; He, J.; Redwing, R.; Gopalan, V.; Churchill, H. O. H.; Lanzara, A.; Samarth, N.; Chang, C.-Z.; Hu, J.; Mao, Z. Q. Evidence for a Magnetic-Field-Induced Ideal Type-II Weyl State in Antiferromagnetic Topological Insulator Mn (Bi 1 − x Sb x) 2 Te 4. *Phys. Rev. X* **2021**, *11* (3), 031032.

(30) Chong, S. K.; Lei, C.; Lee, S. H.; Jaroszynski, J.; Mao, Z.; MacDonald, A. H.; Wang, K. L. Anomalous Landau Quantization in Intrinsic Magnetic Topological Insulators. *Nat. Commun.* **2023**, *14* (1), 4805.

(31) Choe, J.; Lujan, D.; Rodriguez-Vega, M.; Ye, Z.; Leonardo, A.; Quan, J.; Nunley, T. N.; Chang, L.-J.; Lee, S.-F.; Yan, J.; Fiete, G. A.; He, R.; Li, X. Electron−Phonon and Spin−Lattice Coupling in Atomically Thin Layers of MnBi$_2$Te$_4$. *Nano Lett.* **2021**, *21* (14), 6139–6145.

(32) Padmanabhan, H.; Poore, M.; Kim, P. K.; Koocher, N. Z.; Stoica, V. A.; Puggioni, D.; Hugo, H.; Shen, X.; Reid, A. H.; Gu, M.; Wetherington, M.; Lee, S. H.; Schaller, R. D.; Mao, Z.; Lindenberg, A. M.; Wang, X.; Rondinelli, J. M.; Averitt, R. D.; Gopalan, V. Interlayer Magnetophononic Coupling in MnBi2Te4. *Nat. Commun.* **2022**, *13* (1), 1929.

(33) Li, G.; Wu, X.; Gao, Y.; Ma, X.; Hou, F.; Cheng, H.; Huang, Q.; Wu, Y.-C.; DeCapua, M. C.; Zhang, Y.; Lin, J.; Liu, C.; Huang, L.; Zhao, Y.; Yan, J.; Huang, M. Observation of Ultrastrong Coupling between Substrate and the Magnetic Topological Insulator MnBi$_2$Te$_4$. *Nano Lett.* **2022**, *22*, 3856.

(34) Li, J.; Wang, C.; Zhang, Z.; Gu, B.-L.; Duan, W.; Xu, Y. Magnetically Controllable Topological Quantum Phase Transitions in the Antiferromagnetic Topological Insulator MnBi 2 Te 4. *Phys. Rev. B* **2019**, *100* (12), 121103.

(35) Kumar, R.; Session, D. W.; Tsuchikawa, R.; Homer, M.; Paas, H.; Watanabe, K.; Taniguchi, T.; Deshpande, V. V. Circular Electromechanical Resonators Based on Hexagonal-Boron Nitride-Graphene Heterostructures. *Appl. Phys. Lett.* **2020**, *117* (18), 183103.

(36) Chen, C. *Graphene NanoElectroMechanical Resonators and Oscillators*; Columbia University, 2013.

(37) Šiškins, M.; Kurdi, S.; Lee, M.; Slotboom, B. J. M.; Xing, W.; Mañas-Valero, S.; Coronado, E.; Jia, S.; Han, W.; van der Sar, T.; van der Zant, H. S. J.; Steeneken, P. G. Nanomechanical Probing and Strain Tuning of the Curie Temperature in Suspended Cr2Ge2Te6-Based Heterostructures. *Npj 2D Mater. Appl.* **2022**, *6* (1), 1−8.

(38) Badloe, T.; Kim, J.; Kim, I.; Kim, W.-S.; Kim, W. S.; Kim, Y.-K.; Rho, J. Liquid Crystal-Powered Mie Resonators for Electrically Tunable Photorealistic Color Gradients and Dark Blacks. *Light Sci. Appl.* **2022**, *11* (1), 118.

(39) Chen, C.; Deshpande, V. V.; Koshino, M.; Lee, S.; Gondarenko, A.; MacDonald, A. H.; Kim, P.; Hone, J. Modulation of Mechanical Resonance by Chemical Potential Oscillation in Graphene. *Nat. Phys.* **2016**, *12* (3), 240−244.

(40) Morell, N.; Reserbat-Plantey, A.; Tsioutsios, I.; Schädler, K. G.; Dubin, F.; Koppens, F. H. L.; Bachtold, A. High Quality Factor Mechanical Resonators Based on WSe2Monolayers. *Nano Lett.* **2016**, *16* (8), 5102−5108.

(41) Chen, C.; Rosenblatt, S.; Bolotin, K. I.; Kalb, W.; Kim, P.; Kymissis, I.; Stormer, H. L.; Heinz, T. F.; Hone, J. Performance of Monolayer Graphene Nanomechanical Resonators with Electrical Readout. *Nat. Nanotechnol.* **2009**, *4* (12), 861−867.

(42) Lee, J.; Wang, Z.; He, K.; Yang, R.; Shan, J.; Feng, P. X.-L. Electrically Tunable Single- and Few-Layer MoS2 Nanoelectromechanical Systems with Broad Dynamic Range. *Sci. Adv.* **2018**, *4* (3), No. eaao6653.

(43) Chen, B.; Fei, F.; Zhang, D.; Zhang, B.; Liu, W.; Zhang, S.; Wang, P.; Wei, B.; Zhang, Y.; Zuo, Z.; Guo, J.; Liu, Q.; Wang, Z.; Wu, X.; Zong, J.; Xie, X.; Chen, W.; Sun, Z.; Wang, S.; Zhang, Y.; Zhang, M.; Wang, X.; Song, F.; Zhang, H.; Shen, D.; Wang, B. Intrinsic Magnetic Topological Insulator Phases in the Sb Doped MnBi2Te4 Bulks and Thin Flakes. *Nat. Commun.* **2019**, *10* (1), 4469.

(44) Yan, J.-Q.; Okamoto, S.; McGuire, M. A.; May, A. F.; McQueeney, R. J.; Sales, B. C. Evolution of Structural, Magnetic, and Transport Properties in MnBi 2 − x Sb x Te 4. *Phys. Rev. B* **2019**, *100* (10), 104409.

(45) Sass, P. M.; Kim, J.; Vanderbilt, D.; Yan, J.; Wu, W. Robust A -Type Order and Spin-Flop Transition on the Surface of the Antiferromagnetic Topological Insulator MnBi 2 Te 4. *Phys. Rev. Lett.* **2020**, *125* (3), 037201.

(46) Kresse, G.; Furthmüller, J. Efficiency of Ab-Initio Total Energy Calculations for Metals and Semiconductors Using a Plane-Wave Basis Set. *Comput. Mater. Sci.* **1996**, *6* (1), 15−50.

(47) Perdew, J. P.; Burke, K.; Ernzerhof, M. Generalized Gradient Approximation Made Simple. *Phys. Rev. Lett.* **1996**, *77* (18), 3865−3868.

(48) Monkhorst, H. J.; Pack, J. D. Special Points for Brillouin-Zone Integrations. *Phys. Rev. B* **1976**, *13* (12), 5188−5192.

(49) Grimme, S.; Antony, J.; Ehrlich, S.; Krieg, H. A Consistent and Accurate *Ab Initio* Parametrization of Density Functional Dispersion Correction (DFT-D) for the 94 Elements H-Pu. *J. Chem. Phys.* **2010**, *132* (15), 154104.